International Journal of Heat and Mass Transfer 235 (2024) 126181

Contents lists available at ScienceDirect

International Journal of Heat and Mass Transfer

journal homepage: www.elsevier.com/locate/ijhmt

Optimization design and PIV experimental investigation on the heat transfer and flow characteristics in circular tube with oblique wavy tape based on machine learning

Pan Cui, Chunyu Shi, Qinglin Du, Yuhao Zhu, Wei Liu, Zhichun Liu *

School of Energy and Power Engineering, Huazhong University of Science and Technology, Wuhan 430074, China

ARTICLE INFO

Keywords:
Heat transfer enhancement
Oblique wavy tape insert
Longitudinal swirl flow with multi-vortices
Machine learning
Optimization

ABSTRACT

To induce longitudinal swirl flow and enhance heat transfer in heat exchanger tubes, a novel oblique wavy tape insert is introduced in this paper. With identical geometric parameters, the flow and heat transfer characteristics of a tube with V-shaped oblique wavy tape (VOWT) are numerically compared to those of tubes inserted with existing conventional wavy tape (CWT) and center-tapered wavy tape (CTWT). The results show that the VOWT induces larger tangential velocity and a stronger longitudinal swirl flow with two pairs of vortices, effectively reducing flow dead zones. Among the three wavy tapes, the VOWT demonstrates superior heat transfer and overall performance. To expand design space and achieve further performance improvement, multiple types of wavy tape are parameterized into a unified form for optimization. Four geometric parameters of the unified wavy tape are considered as design variables, with the performance evaluation criterion (*PEC*) as the optimization objective. The surrogate model based on machine learning (SML) is employed, which incorporates the Kriging model, genetic algorithm, and machine learning technology. The SML method enhances the local representation of the surrogate model and contributes to improved efficiency. The optimization results show that the optimal wavy tape (OWT) is identified as an oblique wavy tape. Further analysis through field synergy and thermal-hydraulic performance evaluation reveals that the OWT promotes the synergy between velocity and temperature fields. Within the Reynolds number range of 500–1500, heat transfer in the tube with OWT is enhanced by 7.10 to 11.86 times compared to a smooth tube, and the *PEC* ranges from 3.21 to 4.44. This capability of achieving both high heat transfer and overall performance makes oblique wavy tapes suitable for high heat flux scenarios. Finally, the optimized flow field achieved by OWT is verified through a particle image velocimetry (PIV) experiment.

1. Introduction

As fundamental devices for energy transfer and conversion, heat exchanger tubes are found extensive applications [1] in various fields such as chemical engineering, metallurgy, solar energy collection, and waste heat recovery. The performance of heat exchanger tubes significantly influences the overall heat transfer efficiency of the system. Enhancing heat transfer in heat exchanger tubes contributes to improving energy efficiency, curtailing emissions, and diminishing equipment size. Consequently, this area has garnered a surge of research interest in the context of energy conservation and the development of compact apparatuses. Heat transfer enhancement techniques can be categorized into active, passive, and compound methods [2]. Of these, passive techniques, which are devoid of additional external components and offer simplicity in implementation, have gained widespread practical applications. Typical passive methods for tubes encompass the utilization of nanofluids [3], alterations to the tube shape [4], incorporations of artificial roughness such as ribs and grooves [5], and installation of inserts [6]. Particularly, inserts are easily manufactured and assembled, and they can create strong disturbances in the core flow, thereby providing high heat transfer performance [6]. These advantages render them a potent passive augmentation method, especially in laminar flow conditions.

Introducing swirl flow or vortices in tubes can promote the mixing of hot fluids in the boundary region with cold fluids in the core region and disrupt the development of boundary layer, resulting in high heat transfer efficiency [7,8]. By installing twisted tapes, coils, or other

* Corresponding author.
E-mail address: zcliu@hust.edu.cn (Z. Liu).

https://doi.org/10.1016/j.ijheatmasstransfer.2024.126181
Received 14 April 2024; Received in revised form 25 August 2024; Accepted 6 September 2024
Available online 14 September 2024

Nomenclature

A	amplitude of wavy tape (mm)
c_p	specific heat capacity ($J{\cdot}kg^{-1}{\cdot}K^{-1}$)
d_s	displacement (mm)
f	friction factor
h	heat transfer coefficient ($W{\cdot}m^{-2}{\cdot}K^{-1}$)
L	tube length (mm)
L_d	period (mm)
N_a	number of surrogate updating
Nu	Nusselt number
p	pressure (Pa)
PEC	performance evaluation criterion
Δp	pressure drop (Pa)
q	heat flux density ($W{\cdot}m^{-2}$)
Re	Reynolds number
R	tube radius (mm)
r	radial distance (mm)
s	clearance between wavy tape and tube wall (mm)
ΔT	logarithmic mean temperature difference (K)
T	temperature (K)
t	thickness of wavy tape (mm)
u	velocity ($m{\cdot}s^{-1}$)
x, y, z	Cartesian coordinate (m)

Greek symbols

β	synergy angle between velocity and temperature (°)
θ	synergy angle between velocity and pressure (°)
λ	thermal conductivity ($W{\cdot}m^{-1}{\cdot}K^{-1}$)
μ	fluid dynamic viscosity ($kg{\bullet}m^{-1}{\bullet}s^{-1}$)
ρ	density ($kg{\cdot}m^{-3}$)
φ	phase difference (°)

Subscripts

c	center
in	inlet
out	outlet
opt	optimal
max	maximum value
min	minimum value
test	test section
w	wall

Abbreviation

ANN	artificial neural network
CFD	computational fluid dynamics
CTWT	center-tapered wavy tape
CWT	conventional wavy tape
GA	genetic algorithm
OWT	optimal wavy tape
PIV	particle image velocimetry
RBF	radial basis function
RSM	response surface methodology
SML	surrogate model based on machine learning
VOWT	V-shaped oblique wavy tape

vortex generators in tubes is a prevalent way to instigate such flows. Bas et al. [9] experimentally investigated the effects of twisted tape on the thermal and hydraulic performances of a tube. They reported that the heat transfer increased by 0.36–1.79 times with the pressure drop increasing by 1.2–3 times. Harish et al. [10] numerically compared the laminar heat transfer behaviors in tubes with traditional twisted tape and circular protruded twisted tape. The results showed that both the twisted tapes induced swirl flow. The maximal thermal enhancement factor realized by the protruded twisted tape was about 1.5 times that of the traditional twisted tape at the cost of greater flow resistance. Dalkılıç et al. [11] numerically and experimentally examined the heat transfer and pressure drop in tubes with quad-channel twisted tapes. Zhang et al. [12] performed a numerical investigation on the heat transfer and flow characteristics in tubes with multiple regularly spaced twisted tapes. They observed multi-swirling flows and maximum increases of 171 % and 182 % in the Nusselt number by using triple and quadruple twisted tapes, respectively. Akhavan-Behabadi et al. [13] conducted experiments to illustrate heat transfer enhancement by coiled wire inserts in a horizontal tube. Ravikiran et al. [14] adopted a combined insert of a twisted tape with a wire coil and obtained enhanced thermal performance resulting from reversed flow caused by the wire coil, coupled with swirling and impinging flow from the twisted tape. Deshmukh et al. [15] presented an experimental investigation in heat transfer and friction factor characteristics in a tube with a central rod attached with curved delta-wing vortex generators.

Passive methods inevitably lead to an increase in flow resistance while enhancing heat transfer, so striking a balance between the two competing demands for high overall performance is foremost for developing new heat transfer enhancement technologies. Meng et al. [16] and Liu et al. [17-19] conducted theoretical optimization on convective heat transfer inside circular tubes using the filed synergy, entransy dissipation, and exergy destruction, respectively. All their results demonstrate that the optimal flow field structure in circular tubes is longitudinal swirl flow with multi-vortices, which can significantly enhance thermal performance with moderate upswing in flow resistance. To induce such flow, Zheng and Liu et al. [20,21] designed vortex rods and multiple conical strips inserts. Their results showed that both the inserts generated pairs of longitudinal vortices and provided good overall performance. Chamoli et al. [22] developed perforated vortex generators, and a maximum thermal enhancement factor of 1.65 was achieved by the optimized flow field. Wang et al. [23] reported symmetrical wing longitudinal swirl generators, which not only induced longitudinal swirl flow, but also served as a deflector to guide the cold water to scour the tube wall. Liu et al. [24] studied the heat transfer and friction factor in a tube with central slant rods. The results revealed that the new inserts induced multi-longitudinal vortices validated by a particle image velocimetry measurement, and the Nusselt number and friction factor were enhanced by 1.81–5.05 times and 2.49–6.92 times, respectively.

Zheng et al. [25] reviewed the single-phase convective heat transfer enhancement based on multi-longitudinal vortices in heat exchanger tubes. They found that though some techniques could construct multi-longitudinal vortices, they still led to ordinary overall performance, indicating the need for further optimization of the geometries. In addition to the inserts mentioned above, Zhu et al. [26] proposed a newly sinusoidal wavy tape configuration on the basis of wavy strip, and pairs of longitudinal vortices were observed in the tube. However, the overall performance of the tube was mediocre due to the increased flow resistance. Sani et al. [27] compared the performances of solar collectors with twisted tape, wavy tape, and plain tape, respectively. They also found that the overall performance of the tube with wavy tape was general. To reduce flow resistance, Liang et al. [28] designed a center-tapered wavy tape whose centerline was straight. With this structural change, the results showed that the flow resistance was significantly smaller than the tube with conventional wavy tape, rendering an increase in the overall performance. While on the other hand, disturbances to the core area generated by the center-tapered wavy tape were smaller, which weakened the characteristics of swirl

flow and vortices, thus reducing the thermal performance.

In addition to improving geometric structure, parameter optimization is another effective way to strengthen the performance of enhanced tubes. Intelligent optimization algorithms, represented by genetic algorithm (GA) [29], stand out for their global search capability, high efficiency, and wide applicability. These algorithms have found extensive utilization in the optimization of convective heat transfer [30-33], yielding significant improvements in the operating performance. Optimization design involves solving the forward problem, which entails obtaining output physical performance based on input parameters. A frequently employed strategy is to construct a surrogate model based on a certain amount of data to approximate the relationship between inputs and outputs. This method is much more efficient compared to the iterative calculations required in computational fluid dynamics (CFD). Popular surrogate models include artificial neural network (ANN), response surface methodology (RSM), Kriging, and radial basis function (RBF), et al. For instance, Abdollahi et al. [34] conducted an optimization study on winglet vortex generators in a channel to maximize heat transfer while minimizing pressure drop. An ANN-based model was developed, and a multi-objective genetic algorithm was employed to obtain the Pareto front. Zheng and Liu et al. [35] implemented parameter optimization on a vortex rod insert. Combined intelligent algorithm with ANN, the Pareto front and an optimal compromise solution with a heat transfer enhancement factor of 6.57 and friction coefficient ratio of 7.07 was determined. To achieve the maximum overall performance of a channel with curved trapezoidal longitudinal vortex generators, Esmaeilzadeh et al. [36] used GA with ANN to optimize two geometric parameters of vortex generators. Li et al. [37] carried out a numerical optimization on the L twisted tape fitted in heat exchanger tube. Compared to manually designed schemes, the optimal design by GA and RSM achieved a maximum improvement of 25.4 % in the optimization objective.

Despite of high efficiency, these traditional surrogate models encounter several challenges. Firstly, when constructing a surrogate model, design points are typically uniformly distributed across the design space, and the model performance evaluation is usually based on global fitting accuracy. Though this ensures the global performance of the model to some extent, it can lead to distortions in local features, which is particularly problematic for the optimization design of highly nonlinear convective heat transfer. Insufficient model accuracy near the optimal design point can result in deviations between the obtained results and the actual optimal results. Secondly, traditional surrogate models lack a unified criterion for determining the required sample size. Relying on continuous testing of the model performance to decide whether to increase samples brings additional manual work. To address these challenges, Shi et al. [38] proposed the surrogate model based on machine learning method for convective heat transfer optimization. By improving sample distribution through machine learning, iteratively updating the surrogate model, and adding convergence criteria, it can enhance the representation of the surrogate model in local features, decrease the requirement for samples, and reduce manual intervention. This method has demonstrated successful applications in the optimization of artificial roughness [38] and shape [39] of heat exchanger tubes.

According to the literature review, it's found that there are few studies on constructing the optimal flow field structure with wavy tape inserts. The more important is that existing wavy tapes often struggle to achieve both high heat transfer and overall performance, making them may unsuitable for high heat flux scenarios. To fill the gap, this paper introduces oblique wavy tape designed to induce longitudinal swirl flow with multi-vortices inside tubes. Through numerical simulations, the heat transfer and flow characteristics of a tube with V-shaped oblique wavy tape are compared against those of tubes with conventional wavy tape and center-tapered wavy tape. Additionally, the surrogate model based on machine learning is applied to the optimization design of the tube insert. Prior to optimization, multiple types of wavy tape are parameterized into a unified form to expand design space. Subsequently, the tube with obtained optimal wavy tape is carried out field synergy analysis, and the thermal-hydraulic performance is evaluated within the Reynolds number range of 500–1500. Finally, a particle image velocimetry experiment is conducted to validate the flow field structure induced by the optimal wavy tape.

2. Physical model and numerical methods

2.1. Physical model

The schematic of the designed V-shaped oblique wavy tape (VOWT) is illustrated in Fig. 1. As shown, two symmetrically distributed oblique waves converge at the center of the tape, which is periodical along the mainstream direction. The amplitude and period of the central sinusoidal wave are identical to those of the two side waves, but there is a displacement in the z-direction. VOWT is a special case of oblique wavy tape which only requires a displacement between the central and side waves. The insert is fitted in the center of a circular tube with a radius $R = 10$ mm, and a clearance of $s = 1$ mm is reserved between the tape and the tube wall, as shown in Fig. 1(b). To ensure stable flow, the length of the tape is set to $L_0 = 900$ mm. The period and thickness of VOWT are denoted as $L_d = 30$ mm and $t = 1.5$ mm, respectively.

To illustrate the effect of VOWT, the flow and heat transfer characteristics of the tube with VOWT are compared with those of a tube with conventional wavy tape (CWT) proposed by Zhu et al. [26], and a tube with center-tapered wavy tape (CTWT) proposed by Liang et al. [28] under the same operating condition. Fig. 2 provides schematics of the three wavy tapes. CWT exhibits a sinusoidal waveform along the mainstream direction, which can be regarded as a basic form. CTWT consists of sinusoidal curves on both sides of the tape, with the amplitude gradually decreasing towards the center, resulting in a straight centerline.

2.2. Governing equations and boundary conditions

In this paper, the Reynolds number (Re) lies in the range of 500 to 1500, and the flow inside tubes is assumed to be laminar, steady, and incompressible. Water is selected as the working fluid, with constant physical properties specified as follows: density $\rho = 998.2$ kg/m^3, dynamic viscosity $\mu = 1.003 \times 10^{-3}$ kg/(m·s), specific heat capacity $c_p = 4182$ J/(kg·K), and thermal conductivity $\lambda = 0.6$ W/(m·K). The inserts remain rigid without deformation or vibration. Gravity effect, viscous dissipation, and radiative heat transfer are negligible. The governing equations include the mass, momentum, and energy equations which are formulated as Eqs. (1)-(3):

$$\frac{\partial u_i}{\partial x_i} = 0 \tag{1}$$

$$\rho u_i \frac{\partial u_j}{\partial x_i} = -\frac{\partial p}{\partial x_i} + \frac{\partial}{\partial x_i}\left(\mu \frac{\partial u_j}{\partial x_i}\right) \tag{2}$$

$$\rho c_p \left(u_i \frac{\partial T}{\partial x_i}\right) = \lambda \left(\frac{\partial^2 T}{\partial x_i^2}\right) \tag{3}$$

Flow is considered to be fully developed before entering the tube, and the corresponding velocity and temperature profiles at the tube inlet are satisfied with:

$$u(r) = u_c \left[1 - \left(\frac{r}{R}\right)^2\right] \tag{4}$$

$$T(r) = T_c + \frac{qR}{\lambda}\left[\left(\frac{r}{R}\right)^2 - \frac{1}{4}\left(\frac{r}{R}\right)^4\right] \tag{5}$$

where u_c and T_c are the velocity and temperature at the center of the inlet, respectively. u_c depends on Re, while T_c is a constant of 300 K. r is

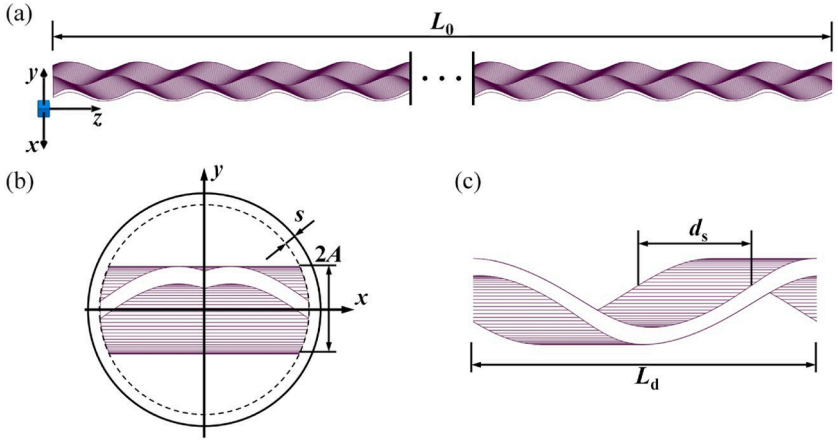

Fig. 1. Configuration and layout of VOWT: (a) three-dimensional view, (b) *z*-direction view, and (c) *x*-direction view of one unit.

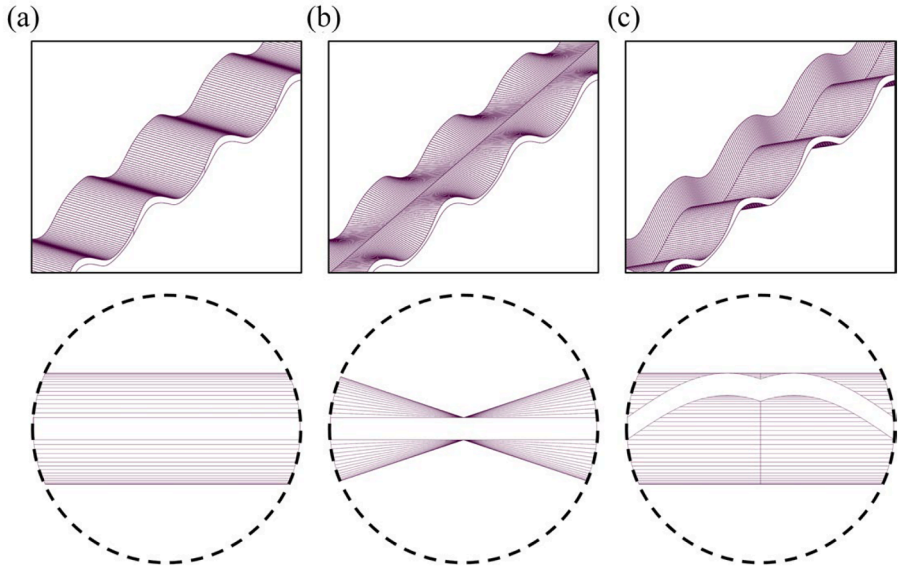

Fig. 2. Schematic diagrams of the three types of wavy tape: (a) CWT, (b) CTWT, and (c) VOWT.

the radial distance, and q is the heat flux on the tube wall fixed to 2000 W/m^2. The tube outlet is set as a pressure outlet and the gauge pressure is 0. A no-slip boundary condition is applied to the walls, and the surfaces of inserts are considered adiabatic.

Numerical simulations are performed on the ANSYS Fluent 19.0 platform, which is based on the finite volume method. The second upwind scheme is employed to discretize the governing equations, and the SIMPLE algorithm is adopted to couple pressure and velocity. The solution process is considered to be converged when the residuals are $<10^{-5}$ for the continuity equation and $<10^{-7}$ for the other equations.

2.3. Data reduction

The Reynolds number *Re* is defined as:

$$Re = \frac{2\rho u_{in} R}{\mu} \tag{6}$$

where u_{in} is the average velocity at the inlet and varies from 0.025 m s^{-1} to 0.075 m s^{-1} depending on *Re*. The friction factor (f) is employed to characterize the hydraulic performance, which can be calculated as:

$$f = \frac{\Delta p}{(1/2)\rho u_{in}^2} \frac{2R}{L} \tag{7}$$

where L represents the length of the test section, and Δp is the pressure drop along it. The Nusselt number (Nu) is chosen to evaluate the thermal performance, which can be calculated as:

$$Nu = \frac{2hR}{\lambda} \tag{8}$$

where h is the heat transfer coefficient and defined as:

$$h = \frac{q}{\Delta T_{test}} \tag{9}$$

ΔT_{test} is calculated with logarithmic mean temperature difference:

$$\Delta T_{test} = \frac{\left(T_w - T_{test,in}\right) - \left(T_w - T_{test,out}\right)}{\ln\left(\frac{T_w - T_{test,in}}{T_w - T_{test,out}}\right)} \tag{10}$$

$$T_{test,in} = \left.\frac{\int_0^R u_{r,z} T_{r,z} r dr}{\int_0^R u_{r,z} r dr}\right|_{z_{in}} \tag{11}$$

$$T_{test,out} = \left.\frac{\int_0^{r_0} u_{r,z} T_{r,z} r dr}{\int_0^{r_0} u_{r,z} r dr}\right|_{z_{out}} \tag{12}$$

Performance evaluation criterion (*PEC*) is employed to assess the overall performance of enhanced tubes, which can be formulated as:

$$PEC = \frac{Nu/Nu_0}{(f/f_0)^{1/3}} \tag{13}$$

where subscript 0 represents the smooth tube under the same operating conditions.

2.4. Grid independence test and model validation

To balance computational efficiency and accuracy, a grid independence test on the tube with VOWT at $Re = 1000$ is conducted to determine an appropriate mesh size. Fluent Meshing 19.0 is used to discrete the computational domain into unstructured Polyhedral grids, and the mesh system is depicted in Fig. 3. The grids near the tube wall and insert surfaces are refined to capture local thermal and hydraulic characteristics. Three sets of mesh systems with different mesh sizes are generated, and the grid numbers are 3.50×10^6, 7.01×10^6, and 12.20×10^6, respectively. According to the numerical results, when the grid number reaches 7.01×10^6, the relative changes of *Nu* and *f* are <1 % compared to the mesh system with 12.20×10^6 grids. This suggests that increasing the grid number beyond 7.01×10^6 has a negligible effect on the simulation results. As a result, the mesh system with 7.01×10^6 grids is adopted for subsequent simulations.

To validate the adopted numerical method, a comprehensive comparison is conducted between the simulation results and theoretical formulas, as well as existing work by Zhu et al. [26]. For the case of a smooth tube operating under laminar flow conditions ($Re < 2100$) with fully developed inlet boundary conditions, the *Nu* and *f* can be derived from the theoretical equations as $Nu_0 = 4.36$ and $f_0 = 64 / Re$ [40], respectively. The comparison between the numerical and theoretical results for the smooth tube is presented in Fig. 4(a). It's found that the maximum relative errors for *Nu* and *f* are 3.14 % and 1.73 %, respectively. To further assess the reliability of the numerical method, a tube model with CWT is developed. The geometric parameters and operating conditions are consistent with Zhu's work [26]. A comparison between the present numerical results and Zhu's data is displayed in Fig. 4(b). It's evident that the two results show good consistency, with maximum relative errors for *Nu* and *f* falling within 3.36 % and 3.76 %, respectively. In summary, the results shown in Fig. 4 demonstrate that the adopted numerical method is accurate and reliable.

3. Flow and heat transfer characteristics analysis

3.1. Comparative analysis of flow characteristics

In order to illustrate the effect of the designed VOWT, a comparative analysis is conducted at $Re = 1000$, examining the flow and heat transfer characteristics of smooth tubes inserted with CWT, CTWT, and VOWT, respectively. A unified amplitude of $A = 3$ mm is set for all three tapes, and other structural parameters, such as thickness *t*, clearance *s*, and period L_d, remain consistent with those described in Section 2.1.

To gain insights into the flow behavior within these tubes, five cross-sections are intercepted equidistantly along the main flow direction within a tube unit where the flow has stabilized. The velocity vector distributions in these cross-sections are shown in Fig. 5. For the tube with CWT, as the fluid flows from the peaks to the valleys of the tape (i.e., from section B to section D), the drainage area above it continuously expands, leading to an adverse pressure region and flow separation. A flow dead zone is formed above the tape, and its area increases progressively. Conversely, below the wavy tape, the diminishing drainage area results in an increase in velocity, which intensifies the local jet effect and reduces the area of flow dead zone here. Similarly, during the flow from the valleys to the peaks of the wavy tape (from section D to section B), the trend of the dead zone changes in the opposite manner. Compared to CWT, CTWT reduces the size of the dead zone to a lesser extent. The transition from a sinusoidal wave to a straight line at the center of the tape not only aids in converging the fluid from both sides towards the center, but also mitigates variations in the flow areas above and below the wavy tape. As a result, the dead zone is almost absent at the center of the tube and primarily exists in the near-wall regions at the ends of the wavy tape. For the tube with VOWT, it's apparent that two pairs of symmetric longitudinal vortices are induced above and below the tape, respectively. The size of these vortices varies with the periodic variation of VOWT. This flow pattern of strong swirl flow with vortices strengthens the fluid mixing between the core flow and boundary flow, further reducing the size of flow dead zone. Upon a comparison of Fig. 5 (a-c), it becomes evident that the VOWT demonstrates the most significant reduction in the flow dead zone, which is primarily concentrated within a very narrow region adjacent to the tape's surfaces. From the velocity vector distributions, it's found that although both the CWT and CTWT introduce tangential velocity into the tubes, their impacts are relatively limited. Consequently, the generated vortices are relatively weak. In contrast, when the tube is inserted with VOWT, the tangential velocity noticeably increases, particularly near the tube wall and insert surfaces. Consequently, the swirl flow and longitudinal vortices are enhanced, realizing a reduced flow dead zone. This enhancement can be attributed to the designed displacement between the central wave and side waves of the tape. The scouring of water on the tube wall is strengthened accordingly, which is conducive to improving the thermal performance.

Fig. 6 shows the streamlines in a longitudinal section segment ($x = 0$) of the three tubes, exhibiting stable flows. By comparing Fig. 6(a-c), it becomes apparent that the CWT and CTWT solely induce localized disturbances within smaller regions, without significantly impacting the dominant flow pattern at the center of the tube. The streamlines in the longitudinal section predominantly remain horizontal. Although the CWT induces a larger disturbance region compared to the CTWT, it leads to a conspicuous increase in the area of low-speed backflow, resulting in greater momentum loss. Conversely, the VOWT provokes the most

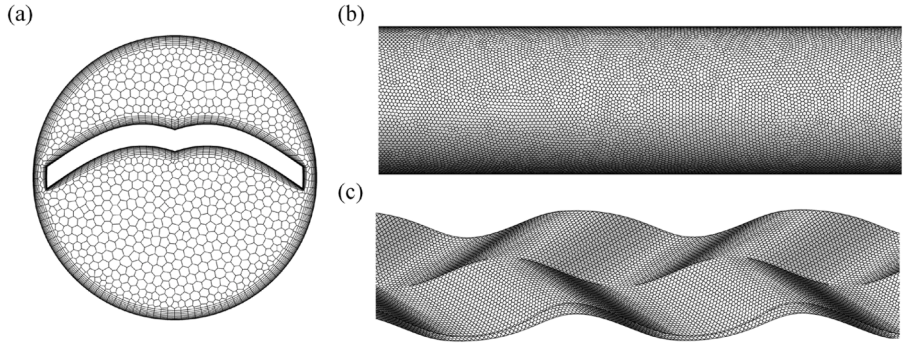

Fig. 3. Mesh system for the tube with VOWT: (a) cross-sectional mesh, (b) tube wall mesh, and (c) wavy tape surface mesh.

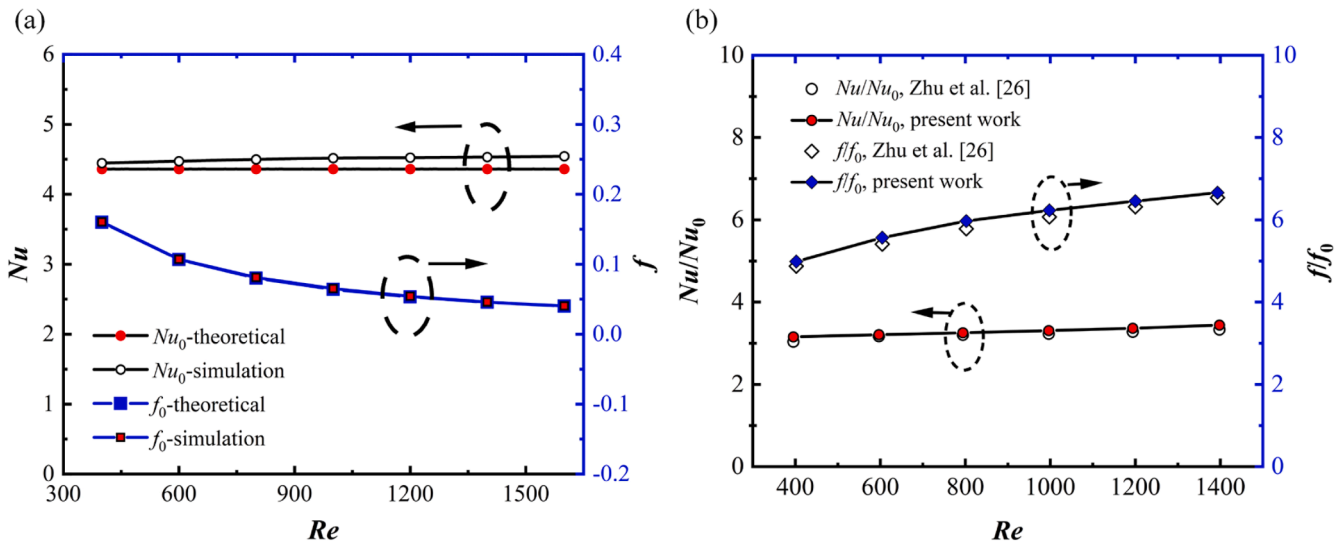

Fig. 4. Numerical model validation: (a) a smooth tube, compared with theoretical formulas and (b) a tube with CWT, compared with Zhu's results [26].

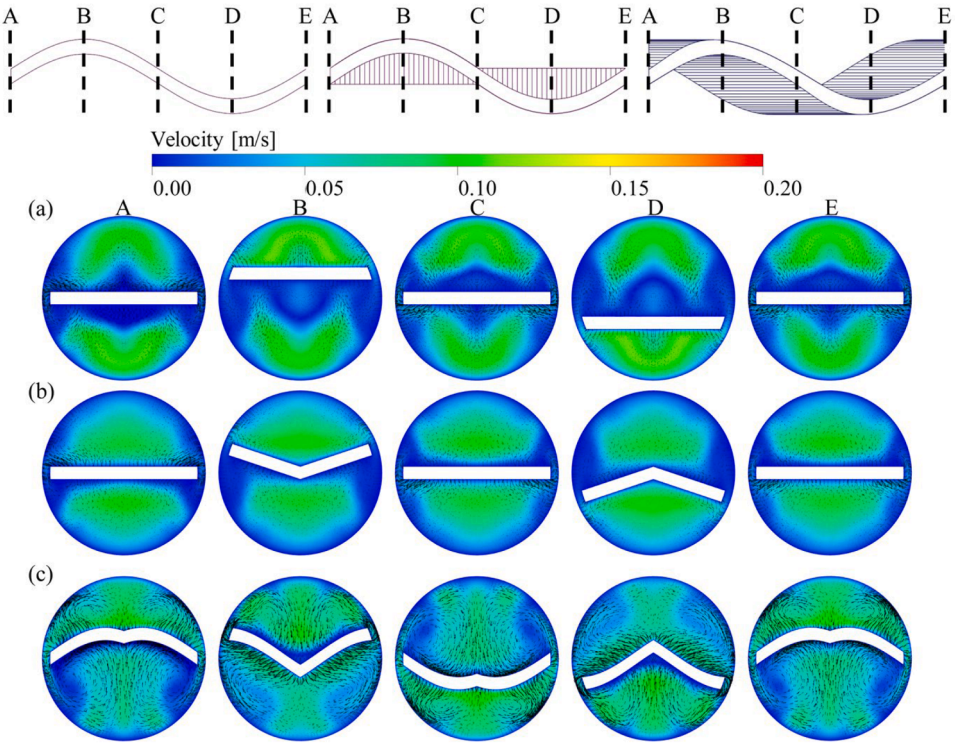

Fig. 5. Velocity vector distributions in five cross-sections: (a) the tube with CWT, (b) the tube with CTWT, and (c) the tube with VOWT.

significant transformation in the flow pattern within the tube, transitioning from horizontal flow to strong swirling flow, effectively diminishing the extent of the backflow region.

The wavy tapes alter the flow field structure within the tube and inevitably have an impact on the flow resistance. To illustrate this, the relative pressure variations along the mainstream direction within two periodic units are plotted in Fig. 7. The pressure at the starting plane is served as the reference point. Among the three wavy tapes, the CWT induces the most pronounced fluctuations in relative pressure due to the most obvious change in the backflow range. The CTWT not only has the smallest disturbance to the core flow, but also does not guide significant tangential velocity. As a result, the tube with CTWT has the lowest relative pressure drop. For the VOWT, owing to its enhanced scouring effect of water on the tube wall and the formation of strong swirl flow, the tube with it experiences heightened frictional resistance and a higher pressure drop.

3.2. Comparative analysis of heat transfer characteristics

The temperature distributions at five cross-sections are presented in Fig. 8, with the cross-sectional positions aligning with those depicted in Fig. 5. By inserting a wavy tape into the core flow region, it induces disturbances in the low-temperature fluid, facilitating the mixing of the low-temperature fluid with the high-temperature fluid near the tube wall, resulting in effectively improved temperature uniformity. It can be observed from Fig. 8 that the development of thermal boundary layers is

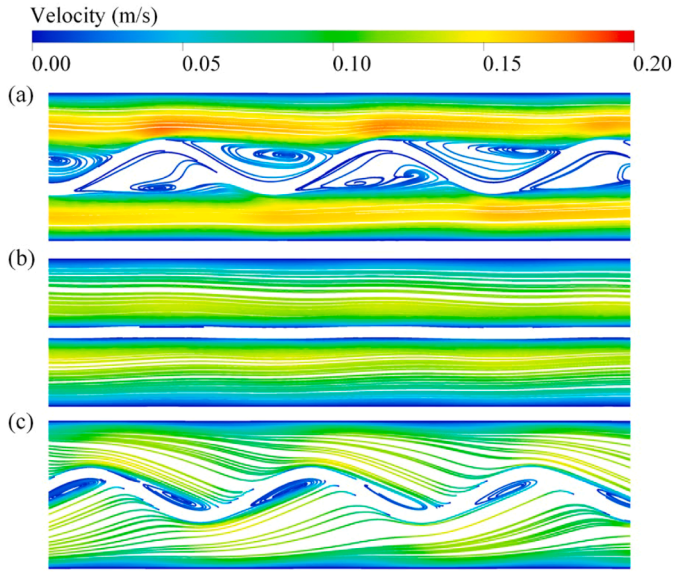

Fig. 6. Streamlines in a longitudinal section segment: (a) the tube with CWT, (b) the tube with CTWT, and (c) the tube with VOWT.

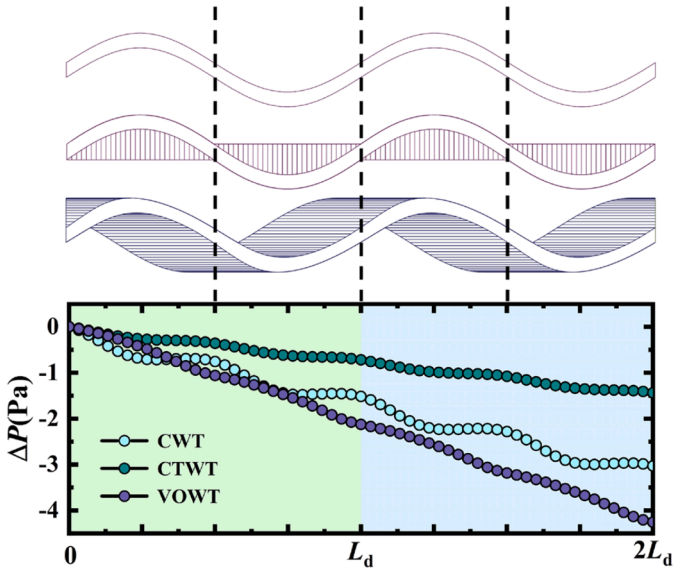

Fig. 7. Relative pressure distributions along the mainstream direction within two periodic units.

disrupted and compressed to exceedingly narrow regions near the tube wall. According to Fig. 8(a and b), the areas near the upper and lower of the tube wall exhibit poor temperature uniformity and reduced temperature gradients, consequently impairing heat transfer efficiency. In contrast, the VOWT not only eliminates the high-temperature regions caused by flow dead zones near the wavy tape, but also significantly reduces the high-temperature regions at the upper and lower of the tube, thereby improving heat transfer.

The local *Nu* distributions within two periodic units are plotted in Fig. 9. Due to the periodic fluctuations of wavy tapes, the periodic transition of the flow state causes the local *Nu* to vary with a period of L_d / 2. In regions where the wavy tapes exhibit larger fluctuations, the ranges of flow dead zones are greater. Therefore, the lowest *Nu* values occur near the peaks or valleys of the wavy tapes. As the flow passes over these peaks or valleys, flow dead zones gradually diminish, leading to enhanced heat transfer until *Nu* reaches its maximum at the point where the amplitude of wavy tapes is zero. When comparing the heat transfer enhancement effects of the three wavy tapes, it's observed that the CTWT acts the weakest enhancement due to the smallest disturbance, followed by the CWT, while the VOWT exhibits significantly superior heat transfer enhancement. This is because the VOWT induces a strong longitudinal swirl flow with multi vortices over a wide range. This flow pattern not only enhances the mixing of fluids but also promotes the scouring of the fluid against the heated wall. Combining this with the relative pressure distribution shown in Fig. 7, the VOWT, despite resulting in a relatively higher pressure drop, brings about significantly improved thermal performance. The *PEC* values for the tubes with CWT, CTWT, and VOWT are 2.95, 3.22, and 3.98, respectively. These results suggest that the VOWT is capable of providing high heat transfer and overall performance for heat exchanger tubes.

4. Optimization and analysis

4.1. Unified parameterization of multiple wavy tapes

In Section 3, the investigation is conducted with fixed structural parameters for the wavy tapes. In order to seek the optimal combination of structural parameters of wavy tape and explore the upper limit of the overall performance of tubes with various wavy tapes, it is essential to undertake parameter optimization on wavy tapes. If the design form of wavy tape is fixed, it will inevitably constrain the optimization space and impose limitations on potential performance improvement. To expand the design space and verify the advantages of oblique wavy tape in heat transfer enhancement, the aforementioned wavy tapes are parameterized into a unified form, after which structural parameter optimization is performed.

Fig. 10 illustrates the variations in the configuration of the unified symmetric wavy tape concerning its design parameters, with the CWT serving as a reference. This unified design is controlled by the centerline and side curves, denoted as f_1 and f_2, respectively. By connecting f_1 and f_2 with straight lines, two design forms can be formed: the CWT and the CTWT. The CWT takes shape when the amplitudes of the sinusoidal curves f_1 and f_2 are equal, represented as $A_1 = A_2 = A$. The CTWT is formed when f_1 is a straight line and f_2 is a sinusoidal curve, i.e., $A_1 = 0$, $A_2 = A$. Notably, the VOWT deviates from the CWT and CTWT by introducing a displacement along the mainstream direction for f_1 and f_2, denoted as d_s. This displacement results in an included angle between the connecting lines of f_1 and f_2 and the cross-section of the tube. These three design forms of wavy tape can be unified with the three parameters. To further broaden the design space, the initial phase difference φ between f_1 and f_2 is also taken into account. Consequently, by manipulating four structural parameters (A_1, A_2, d_s, φ), it becomes feasible to achieve a unified design encompassing multiple forms of wavy tape.

Design ranges of the four parameters are as follows: $0 \le A_1, A_2 \le 5.5$ mm, $0 \le \varphi \le 15^\circ$, and $0 \le d_s \le 10$ mm, respectively. Keeping other structural parameters fixed, the optimization objective is to maximize the *PEC* of the tube at $Re = 1000$.

4.2. Surrogate model based on machine learning

The surrogate model based on machine learning (SML) is adopted to optimize the unified wavy tape, making the first application of SML in tube insert optimization. The most significant difference between SML and traditional surrogate models is that it dynamically expands the dataset through machine learning and updates the surrogate model until convergence, rather than trained once. This iterative process allows for the enhancement in the local feature representation capability of the surrogate model, particularly near the optimal solution, while preserving global accuracy. Moreover, the SML method can effectively reduce sample requirement, thus improving optimization efficiency.

The primary process of SML in this study is illustrated in Fig. 11. Initially, 40 uniformly distributed sample points are determined through

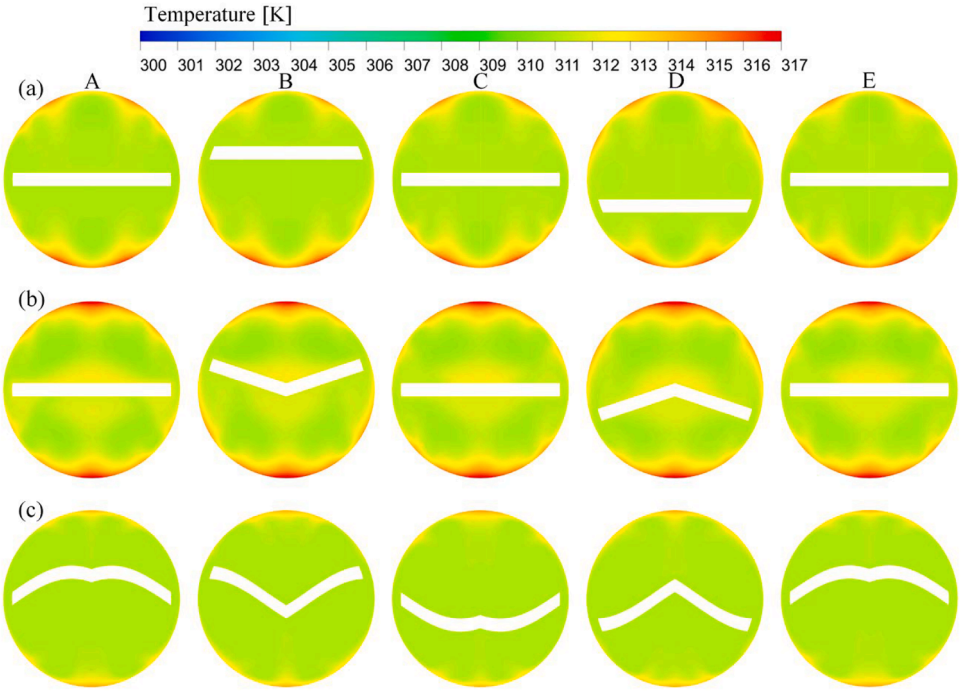

Fig. 8. Temperature distributions in five cross sections: (a) the tube with CWT, (b) the tube with CTWT, and (c) the tube with VOWT.

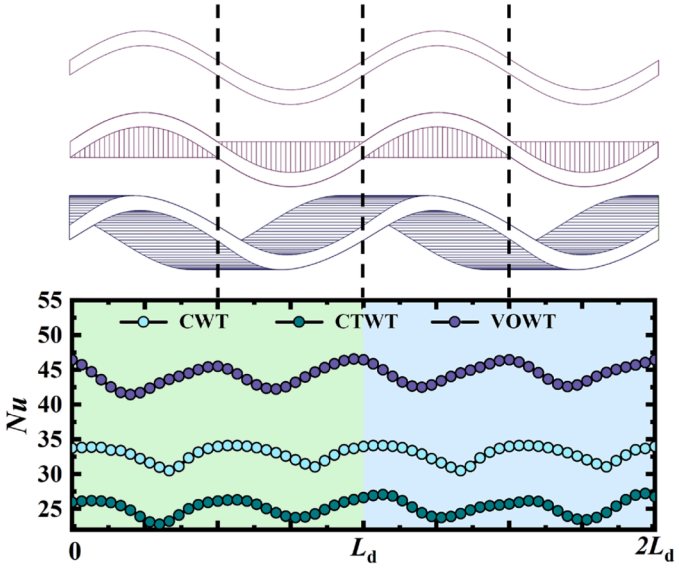

Fig. 9. Local *Nu* distributions within two periodic units.

Latin hypercube sampling and solved by numerical simulation. The specific information of the obtained initial dataset is presented in Table 1 below. These 40 sets of data are then used to train a preliminary surrogate model based on the Kriging, which is developed using MATLAB in this paper. For a given input $\mathbf{x}$, the output $\boldsymbol{Y}(\mathbf{x})$ of a Kriging model meets a normal distribution with a mean of $\hat{y}(\mathbf{x})$ and a variance of $s(\mathbf{x})$ [41], expressed as follows:

$$Y(\mathbf{x}) \sim N(\hat{y}(\mathbf{x}), s(\mathbf{x})) \tag{14}$$

The key of SML hinges upon the methodology for determining new sampling points. Both the minimum value (corresponding to the optimal solution) of the current surrogate model and the model's uncertainty significantly influence the selection of candidate point. The former signifies the extent to which the optimal result is improved, while the latter determines the likelihood of improvement. Assuming the minimum value of the current model is $f_{\min}$, the improvement quantity $I(\mathbf{x})$ is defined as:

$$I(\mathbf{x}) = \max[f_{\min} - \hat{y}(\mathbf{x}), 0] \tag{15}$$

Furthermore, the expected value of $I(\mathbf{x})$, denoted as $EI(\mathbf{x})$, can be obtained [38]:

$$EI(\mathbf{x}) = \int_{-\infty}^{f_{\min}} (f_{\min} - \hat{y}(\mathbf{x})) \frac{1}{\sqrt{2\pi}s(\mathbf{x})} \exp\left(-\frac{\hat{y}(\mathbf{x})^2}{2s(\mathbf{x})^2}\right) \mathrm{d}Y \tag{16}$$

This equation can be further simplified as:

$$EI(\mathbf{x}) = (f_{\min} - \hat{y}(\mathbf{x}))\Phi\left(\frac{f_{\min} - \hat{y}(\mathbf{x})}{s(\mathbf{x})}\right) + s(\mathbf{x})\phi\left(\frac{f_{\min} - \hat{y}(\mathbf{x})}{s(\mathbf{x})}\right) \tag{17}$$

where $\Phi(\cdot)$ and $\phi(\cdot)$ represent for the cumulative distribution function and probability density function of standard normal distribution, respectively. It can be observed that $EI(\mathbf{x})$ is affected by both the optimal result of the current surrogate model and the distribution of errors. A higher EI value indicates a smaller $\hat{y}(\mathbf{x})$ and/or a larger $s(\mathbf{x})$. Therefore, maximizing $EI(\mathbf{x})$ is adopted as the criterion for adding new sampling points. During the updating of the surrogate model, the maximum value of $EI(\mathbf{x})$ gradually decreases, suggesting the stabilization of the predicted optimal solution and a concurrent reduction in prediction error.

In the described procedure, $f_{\min}$ is obtained through the widely applied genetic algorithm (GA). It offers several advantages, including high efficiency, broad applicability, and global search capability. The specific parameter settings for GA are outlined in Table 2. The information of the newly determined sampling point is subsequently passed to the CFD solver to obtain the output. This input and output data pair is then utilized to update the surrogate model. These two processes of adding data point and updating surrogate model alternate until convergence.

4.3. Optimization results and analysis

4.3.1. Optimization results

Optimization is considered converged when the optimal *PEC*

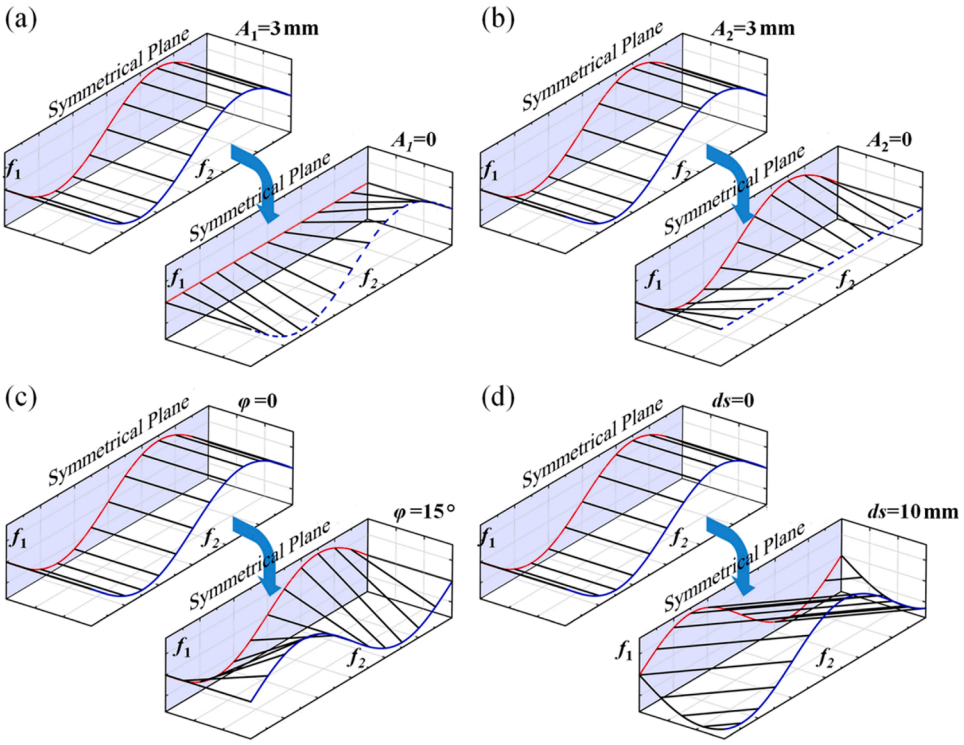

Fig. 10. Variations of the unified wavy tape surface with respect to design parameters: (a) the amplitude of centerline, A_1, (b) the amplitude of side curves, A_2, (c) the initial phase difference, φ, and (d) the displacement, d_s.

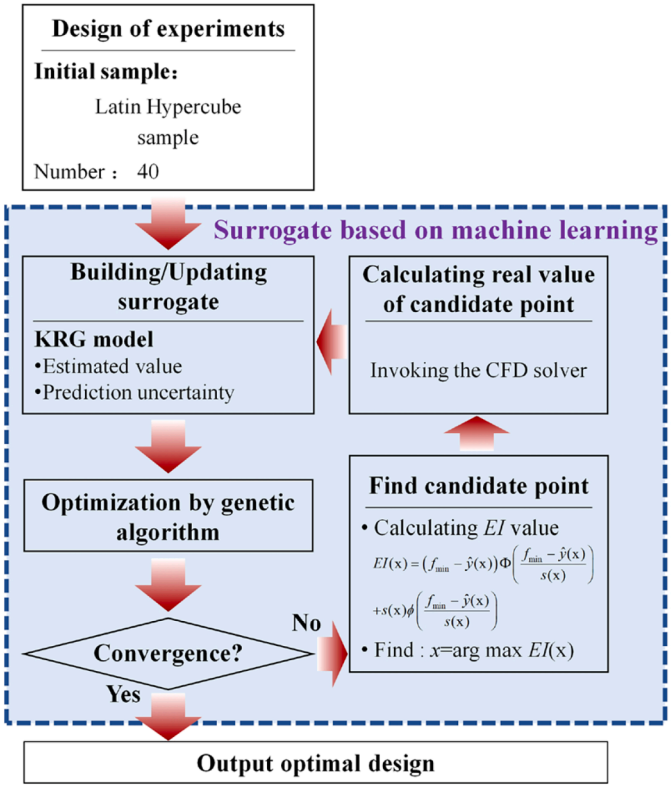

Fig. 11. Framework of the surrogate model based on machine learning.

(PEC_{opt}) remains unchanged for 20 consecutive steps and the maximum of $EI(\mathbf{x})$ (EI_{max}) falls below 10^{-4}. Variations of PEC_{opt} and EI_{max} during the optimization process are illustrated in Fig. 12. As expected, EI_{max} generally exhibits a downward trajectory due to reductions in the model uncertainty and improvement quantity of the objective. After 56 iterations of surrogate model updates, PEC_{opt} stabilizes at 4.099 and does not change. Upon the addition of 91 design points, EI_{max} descends below 10^{-4}, signifying the completion of optimization.

The geometric parameters of the obtained optimal design are as follows: $A_1 = 3.163$ mm, $A_2 = 2.221$ mm, $\varphi = 1.270°$, and $d_s = 8.963$ mm. Due to the coupling between the CFD solver and the surrogate model, the predicted optimal solution is obtained as a candidate point that has been simulated by CFD, thus eliminating prediction errors. Despite having a similar dataset size, the optimal result obtained through this method is more accurate than those by traditional surrogate models [42,43]. Moreover, the SML offers flexibility to conveniently control the prediction accuracy of optimal result by adjusting convergence criteria. When aiming for an equivalent level of prediction accuracy as traditional surrogate models, the SML can reduce the sample requirement and improve the efficiency of optimization design through reasonable adjustments to sample distribution.

The configuration of the optimal wavy tape (OWT) is depicted in Fig. 13, which is demonstrated as an oblique wavy tape. The relatively large displacement d_s indicates its significant role in improving the overall performance of the tube, primarily by inducing enhanced tangential velocity and swirl flow. Furthermore, it is noticed that the amplitude A_1 of the wavy tape centerline is slightly larger than that of the side curves A_2. This variance in amplitude aids in imparting tangential velocity to the fluid and facilitates the formation of longitudinal vortices.

4.3.2. *Field synergy analysis*

To elucidate the reasons behind the superior overall performance of the tube with OWT, the field synergy theory is employed to analyze the optimization results. Field synergy theory, originally proposed by Guo et al. [44], provides an interpretation of the physical mechanism underlying the enhancement of convective heat transfer by examining the synergy between the velocity and temperature fields. Liu et al. [45]

Table 1
Latin hypercube sampling designs and corresponding results.

No.	A_1(mm)	A_2(mm)	φ(°)	ds(mm)	Nu	f	PEC
1	3.40	5.19	1.96	1.94	36.882	1.382	3.038
2	0.23	4.34	4.87	5.88	39.766	0.776	3.970
3	2.01	2.63	6.16	5.57	36.476	0.668	3.829
4	0.36	0.24	5.55	0.19	6.061	0.199	0.953
5	0.70	2.82	13.52	5.42	25.678	0.395	3.210
6	0.09	0.47	11.74	7.41	6.708	0.198	1.057
7	4.74	1.47	11.51	8.59	22.773	0.558	2.537
8	5.34	3.14	10.35	6.48	23.932	0.731	2.437
9	2.21	0.64	1.44	2.31	23.982	0.379	3.040
10	3.47	4.23	0.18	9.87	48.219	1.792	3.642
11	3.87	3.91	8.78	3.07	42.698	1.009	3.905
12	4.95	2.99	9.01	4.63	44.866	1.100	3.988
13	1.63	5.06	5.66	9.50	42.828	1.059	3.855
14	4.00	4.61	2.73	2.02	38.527	1.544	3.058
15	0.97	4.51	7.53	3.37	41.033	0.842	3.986
16	2.16	0.06	13.25	0.37	21.677	0.276	3.056
17	0.61	5.49	14.49	6.56	39.764	0.817	3.902
18	4.89	1.86	4.85	4.44	24.830	0.762	2.494
19	2.35	0.69	3.48	1.52	18.802	0.305	2.564
20	4.26	1.28	1.54	9.48	40.728	1.060	3.665
21	1.81	3.23	3.09	1.11	38.592	0.832	3.765
22	5.50	0.39	8.55	6.18	24.875	0.731	2.534
23	1.72	2.42	0.02	7.59	36.801	0.699	3.804
24	0.53	5.35	4.24	3.65	40.129	1.002	3.679
25	2.71	2.52	7.01	6.89	22.898	0.443	2.756
26	4.48	1.72	7.28	4.24	40.943	0.989	3.770
27	3.74	1.21	12.08	2.62	22.863	0.450	2.737
28	0.85	1.59	2.56	7.07	24.617	0.394	3.080
29	5.20	3.47	4.38	1.36	37.207	1.692	2.865
30	4.40	4.76	14.26	7.97	24.872	0.481	2.912
31	1.37	2.09	9.72	0.76	14.433	0.281	2.021
32	2.84	0.83	10.11	8.06	25.798	0.459	3.067
33	3.25	1.99	14.16	4.93	16.508	0.321	2.213
34	1.13	4.89	11.23	2.93	30.148	0.562	3.351
35	3.03	3.69	0.85	3.96	32.484	0.849	3.148
36	4.57	3.36	6.13	8.78	30.131	0.954	2.808
37	2.53	4.06	12.11	8.48	26.134	0.477	3.068
38	2.92	3.84	7.69	5.02	30.181	0.690	3.133
39	3.64	2.29	13.37	0.61	22.284	0.422	2.726
40	1.44	1.06	11.10	9.05	17.096	0.279	2.400

Table 2
Parameter settings of genetic algorithm.

Parameters	Value
Population size	300
Crossover fraction	0.8
Mutation fraction	0.2
Maximum generations	500
Maximum stall generation	20
Termination tolerance	10^{-6}

further developed it to the multi-field synergy principle to comprehensively evaluate the intensity of heat transfer and flow. According to the multi-field synergy principle, the synergy angle β between velocity $\boldsymbol{U}$ and temperature gradient ∇T, as well as the synergy angle θ between $\boldsymbol{U}$ and pressure gradient ∇p, can be formulated as follows:

$$\beta = \arccos\frac{\boldsymbol{U}\cdot\nabla T}{|\boldsymbol{U}||\nabla T|} \tag{18}$$

$$\theta = \arccos\frac{\boldsymbol{U}\cdot\nabla p}{|\boldsymbol{U}||\nabla p|} \tag{19}$$

Reducing β improves the synergy between velocity and temperature gradient and enhances heat transfer. Similarly, a smaller θ represents an improved synergy between velocity and pressure gradient, leading to reduced flow resistance.

Fig. 14 shows the distributions of the synergy angle β and velocity vectors at four equidistant cross-sections within one unit of the tube with OWT. It is evident that the OWT induces two pairs of strong longitudinal vortices. Additionally, β falls below 90° in specific regions. This is because the OWT generates velocity components perpendicular to the mainstream direction, aligning the velocity vectors more closely with the direction of temperature gradients. It's revealed that the OWT improves the synergy between the velocity and temperature fields, resulting in enhanced heat transfer.

Distributions of the synergy angle θ at the four cross-sections are presented in Fig. 15. The OWT intensifies the flow and induces local flow separations, weakening the synergy between velocity and pressure fields and leading to increased local θ. Comparing the distributions of β and θ, a noteworthy observation emerges: the regions with decreased β and increased θ exhibit a substantial overlap, primarily located near the centers of longitudinal vortices. It suggests that while the longitudinal vortices enhance the synergy between velocity and temperature, they also attenuate the synergy between velocity and pressure to some extent. This dual effect corresponds to an enhancement in heat transfer, accompanied by an increase in flow resistance.

To quantitatively assess the performance differences among tubes with OWT, CWT, and CTWT, Fig. 16 provides comparisons of the volume-averaged synergy angles β and θ, as well as the performance parameters Nu and f. Due to small disturbances to the fluid and minimal effect on the mainstream flow, the tube with CTWT exhibits poor synergy between the flow and temperature fields, ultimately yielding the weakest heat transfer performance, characterized by the smallest Nu value of about 25. The tube with OWT has the smallest synergy angle β, indicating the best synergy between velocity and temperature fields. As a result, it achieves the highest Nu value, which is about 1.8 times that of the tube with CTWT. The size relationships of synergy angle θ and friction factor f of the three tubes are opposite to those of β and Nu. The tube with CTWT has the smallest synergy angle θ and the lowest flow resistance, followed by the tube with TWT. The OWT leads to significant increases in local θ due to enhanced longitudinal vortices, resulting in a larger average θ and increased flow resistance. Nevertheless, this increase is quite worthwhile due to the significantly enhanced heat transfer.

4.3.3. Performance evaluation

In order to comprehensively compare the thermal-hydraulic performance of the three enhanced tubes under variable flow conditions, performance evaluation on them is conducted within the Re range of 500–1500. As depicted in Fig. 17, the heat transfer enhancement ratio (Nu / Nu_0), the friction factor ratio (f / f_0), and the PEC of the three tubes all exhibit an increasing trend with rising Re. This trend indicates that the wavy tapes exert more pronounced and efficient enhancement effects as the flow intensifies. However, the enhancement extents of the three wavy tapes are different. The OWT achieves the most significant and efficient enhancement, and the tube with OWT consistently exhibits the highest Nu / Nu_0 at the expense of the highest f / f_0. On the other hand, the CTWT provides the weakest enhancement effect, with small growth rates in Nu / Nu_0 and f / f_0 as Re increases. The enhancement effect by the CWT falls between those by the OWT and CTWT, while the tube with it experiences the largest growth rate in f / f_0 due to significant backflow regions. Notable, as Re reaches 1500, the flow resistance caused by the CWT approaches that by OWT. Nonetheless, the OWT induces a stronger longitudinal swirl flow with multi-vortices and achieves more efficient heat transfer, so the overall performance of the tube with OWT significantly surpasses that of the tube with CWT. Moreover, as shown in Fig. 17(c), the tube with OWT consistently maintains the highest PEC values across the investigated Re range, demonstrating a noticeable superiority over the other two enhanced tubes. Within the Re range of 500–1500, the Nu / Nu_0 of the tube with OWT ranges from 7.10 to 11.86, the f / f_0 ranges from 10.83 to 19.09, and the PEC ranges from 3.21 to 4.44. These results reveal that under laminar flow conditions, the oblique wavy tape, represented by the OWT, is capable of achieving high heat transfer and moderate flow resistance, thus providing excellent

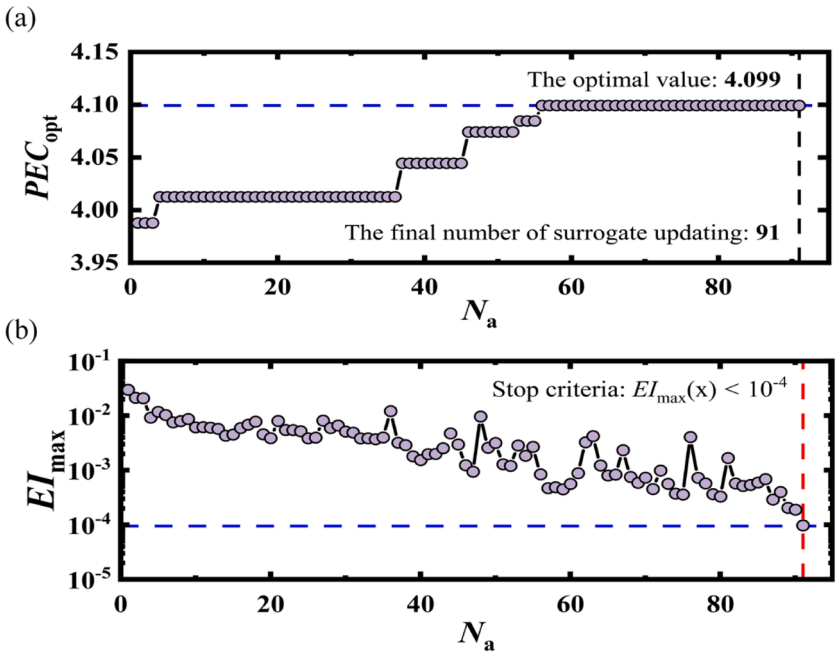

Fig. 12. Variations of: (a) the optimal *PEC*, PEC_{opt} and (b) the maximum of *EI*(x), EI_{max} with the number of surrogate updating N_a.

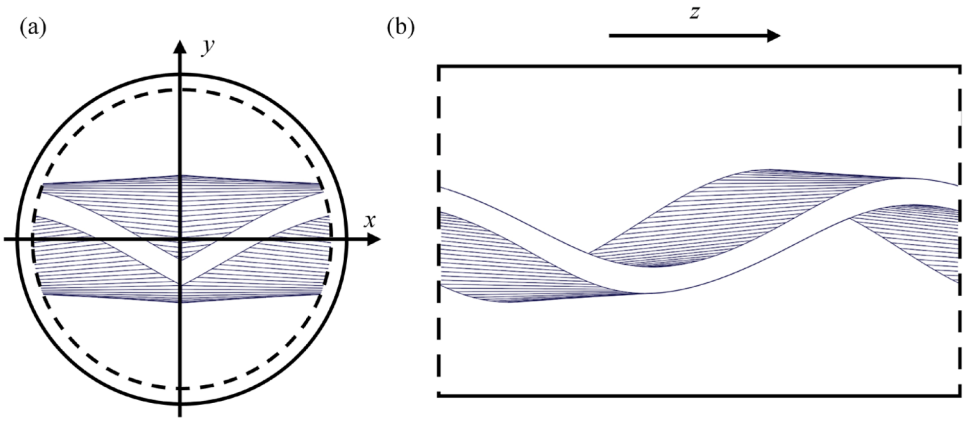

Fig. 13. Diagram of the obtained optimal wavy tape: (a) *x*-direction view and (b) *z*-direction view.

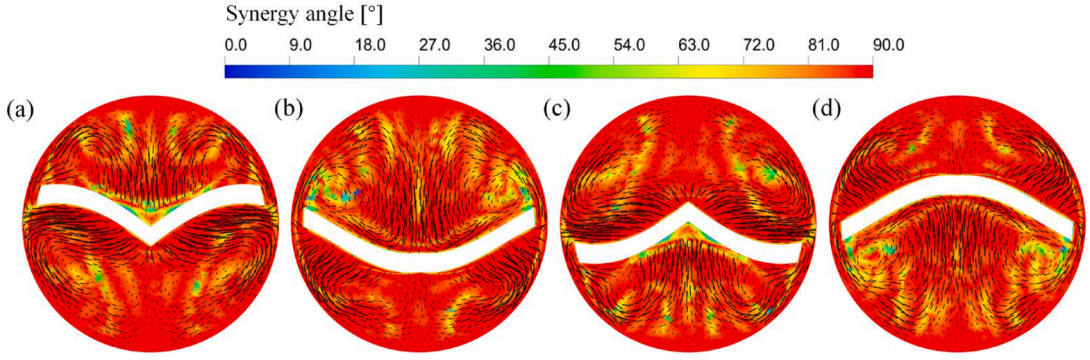

Fig. 14. Distributions of synergy angle β and velocity vectors at 4 cross-sections of the tube with OWT.

overall performance. It can be considered that the oblique wavy tape is more suitable for high heat flux scenarios than existing conventional and center-tapered wavy tapes.

5. PIV experiment verification

The enhanced performance of the tube with OWT hinges on the alteration of flow pattern. Therefore, it is imperative to conduct an

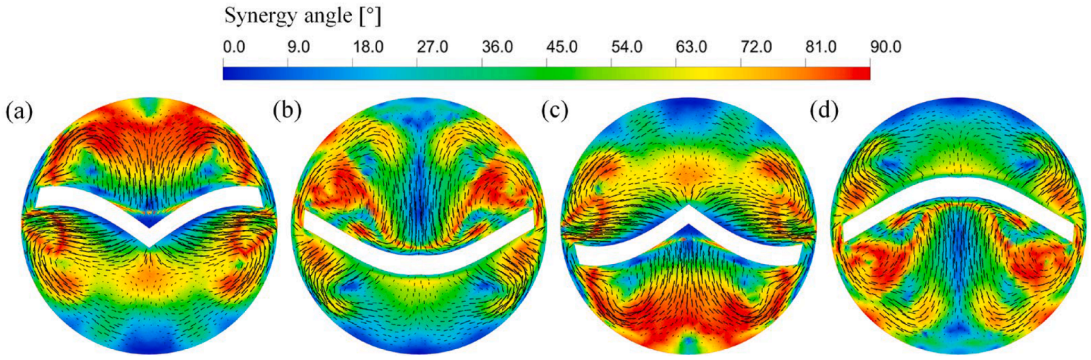

Fig. 15. Distributions of synergy angle θ and velocity vectors at 4 cross-sections of the tube with OWT.

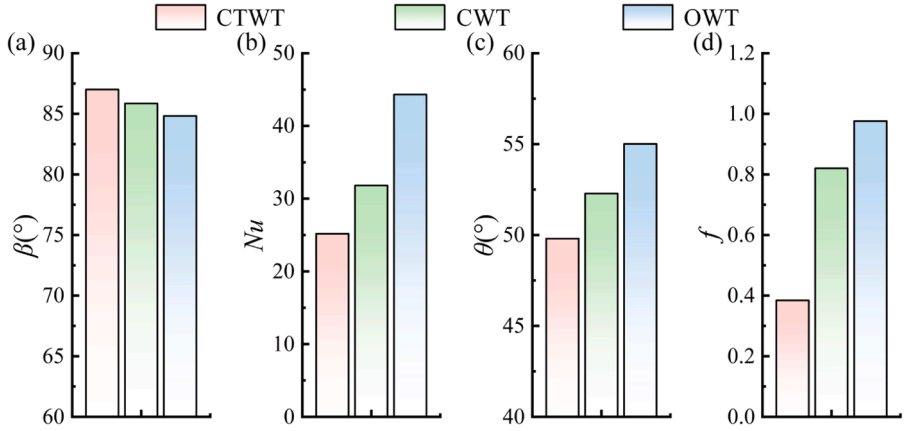

Fig. 16. Comparisons of average synergy angles and performance of the three enhanced tubes: (a) β, (b) Nu, (c) θ, and (d) f.

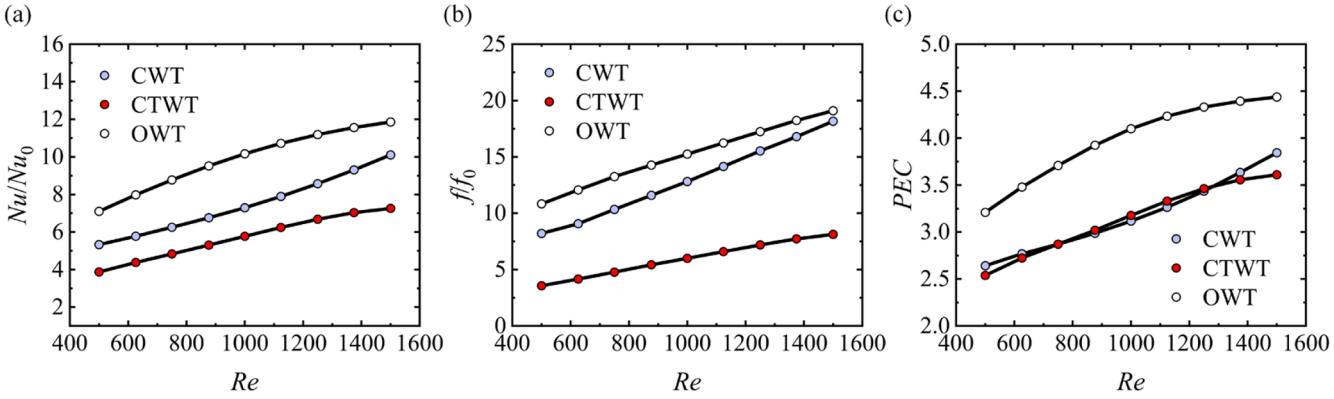

Fig. 17. Performance evaluation on the three enhanced tubes at different Re numbers: (a) Nu / Nu_0, (b) f / f_0, and (c) PEC.

experimental measurement to verify the induced flow field. In this work, particle image velocimetry (PIV) is employed to measure the flow field structure within a tube fitted with OWT, and the results are compared with those from numerical simulation.

The used stereoscopic-PIV system is presented in Fig. 18, which can provide both the two-dimensional flow field and the velocity distributions along the main flow (z-direction) at the measured cross-section. The corresponding system schematic is illustrated in Fig. 19. The experimental system mainly consists of a test tube system, a water supply system, a laser and synchronizer system, as well as a data acquisition and analysis system. There is an upstream tube labeled 5 in Fig. 19 to confirm that the flow is fully developed before entering the test section. The main experimental components and devices are displayed in Fig. 20. Two POWERVIEW™ Plus 4MP cameras with a resolution of 2048 × 2048 are applied to capture flow images. The Nd: YAG laser generator with a group of lenses is used to generate the light sheet. The FLUOSTAR Rhodamine B particles produced by EBM corporation are adopted as tracer particles, with an average particle size of 15 μm and a density of 1.1 g/cm^3. The dimensions of the test tube and the OWT are consistent with the optimization results. The wavy tape is made of curable resin through additive manufacturing, as shown in Fig. 20(e). Protrusions are designed on both sides of the tape to fix it, preventing it from moving due to the impact of working fluid. The test water box, test tube, and water prisms are made of transparent acrylic glass to ensure good light transmission and accurate measurement results.

Before formal measurement, a spatial calibration using a calibration

Fig. 18. The stereoscopic-PIV test system.

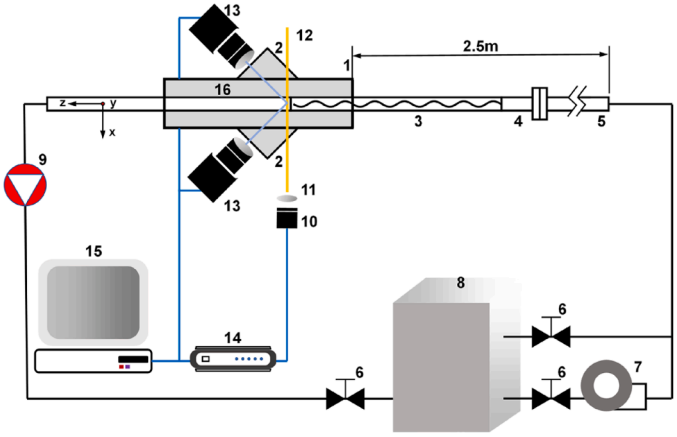

Fig. 19. Schematic of the stereoscopic-PIV system: 1. test water box, 2. water prism, 3. test tube section, 4. entrance development section, 5. upstream tube, 6. control valves, 7. water pump, 8. water tank, 9. electromagnetic flowmeter, 10. laser, 11. Lenses, 12. light sheet, 13. CCD cameras, 14. Synchronizer, 15. computer, 16. observation tube section.

board is carried out to ensure precise alignment of the imaging plane of the cameras with the light sheet. Throughout the experiment, the ambient temperature is maintained at 300 K, so the physical properties of the adopted distilled water are similar to those used in the numerical simulation. Moreover, an electromagnetic flowmeter is used to ensure a flow condition of $Re = 1000$. After the experiment, 800 images recorded are used to calculate the average vector fields with the DaVis 8.4 software. In this process, the interrogation window size is 32 × 32 pixels with a 50 % overlap.

Fig. 21 displays a comparison of the numerical and experimental velocity vector distributions at the observation section. It can be observed that the velocity vector distributions measured by the PIV experiment generally agree well with the numerical results. Both of them exhibit two pairs of longitudinally vortex structure. The longitudinal vortices on the lower side are relatively larger, while those on the upper side are smaller. Some discrepancies between the numerical and experimental results are mainly observed near the tube wall, which may be attributed to the reflection of the tube wall and disturbances caused by the protrusions of the wavy tape. In addition to the velocity vector distributions, the contours of velocity and absolute error between numerical and experimental results at the observation section are illustrated in Fig. 22. This visual representation reinforces the consistency between the simulation and experimental data. As depicted in Fig. 22(c), the absolute error is very small throughout most areas. The maximum absolute error in velocity is below 0.02 m s^{-1}, and the mean square error is 7.00 × 10^{-5} m^2/s^2. In summary, the experimental results affirm the accuracy of numerical results, conclusively verifying the generation of a longitudinal swirl flow with multi-vortices induced by the OWT.

6. Conclusion

In this paper, a novel oblique wavy tape insert is proposed for convective heat transfer enhancement of heat exchanger tubes. A numerical comparison is carried out between the flow and heat transfer characteristics of tubes with existing conventional wavy tape (CWT), center-tapered wavy tape (CTWT), and newly designed V-shaped oblique wavy tape (VOWT). Furthermore, the three types of wavy tape are parameterized into a unified form, and an optimization design is conducted on it employing the surrogate model based on machine learning (SML). The tube with the obtained optimal wavy tape (OWT) is then subjected to filed synergy analysis and thermal-hydraulic performance evaluation. Additionally, a PIV experiment is conducted to validate the flow field of the tube with OWT. Main conclusions can be drawn as follows:

(1) Compared to the CWT and CTWT, the VOWT leads to an increase in the tangential velocity of the fluid, inducing stronger longitudinal swirl flow with two pairs of vortices. This improvement in the flow field significantly reduces flow dead zones, improves temperature uniformity of fluid, and enhances the scouring of water on the tube wall, providing higher heat transfer and overall performance.
(2) The SML method is successfully applied in the optimization design of tube insert, exhibiting high accuracy and efficiency. With the performance evaluation criterion (*PEC*) as the optimization objective, the OWT is obtained in the form of an oblique wavy tape. Field synergy analysis shows that the induced longitudinal vortices enhance the synergy between velocity and temperature fields.
(3) The thermal-hydraulic performance evaluation on the tube with OWT reveals its high heat transfer and moderate flow resistance, thus achieving excellent overall performance. Within the Reynolds number range of 500–1500, heat transfer is enhanced by 7.10 to 11.86 times with the friction factor increasing by 9.83 to 18.09 times compared to a smooth tube, yielding a *PEC* ranging from 3.21 to 4.44. This characteristic of providing both high heat transfer and overall performance makes oblique wavy tape more suitable for high heat flux scenarios, addressing deficiencies in the performance enhancement of existing wavy tapes.
(4) The optimized flow field structure in the tube induced by the OWT is verified through a PIV test, demonstrating the generation of a longitudinal swirl flow with multi-vortices.

Data availability

No data was used for the research described in the article.

CRediT authorship contribution statement

Pan Cui: Writing – original draft, Methodology, Conceptualization, Data curation, Software. **Chunyu Shi:** Writing – original draft, Methodology, Conceptualization. **Qinglin Du:** Data curation, Software. **Yuhao Zhu:** Investigation, Writing – review & editing. **Wei Liu:** Supervision, Conceptualization. **Zhichun Liu:** Conceptualization, Investigation, Writing – review & editing, Funding acquisition.

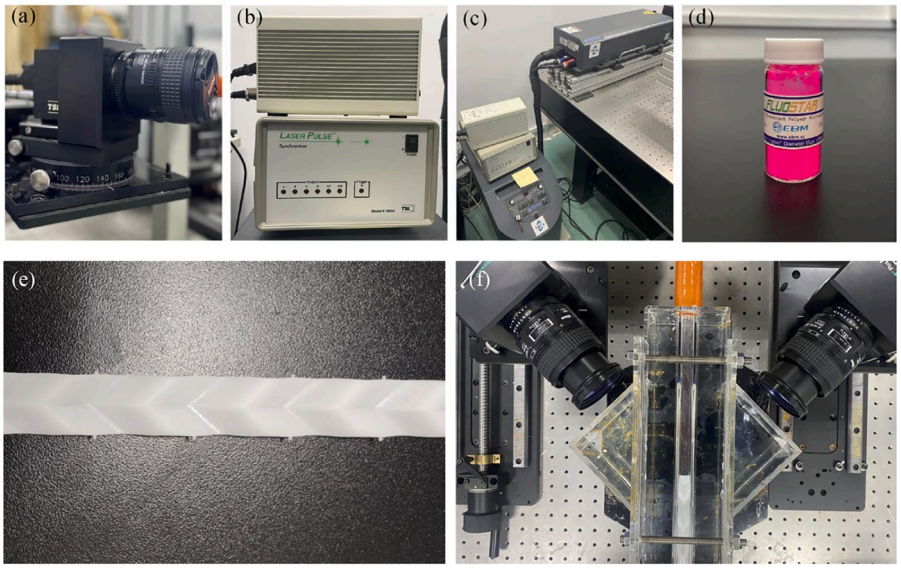

Fig. 20. (a) CCD camera, (b) synchronizer, (c) double pulse laser machine, (d) tracer particles, (e) wavy tape insert, and (f) test and observation tube section.

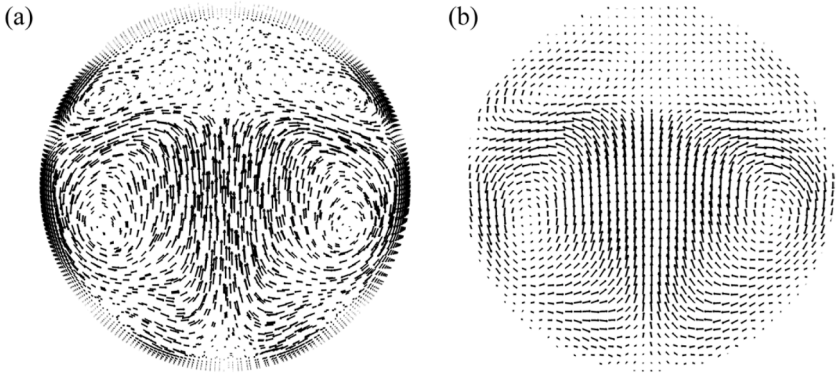

Fig. 21. Comparison of the velocity vectors at the observation section: (a) numerical simulation, and (b) PIV experiment.

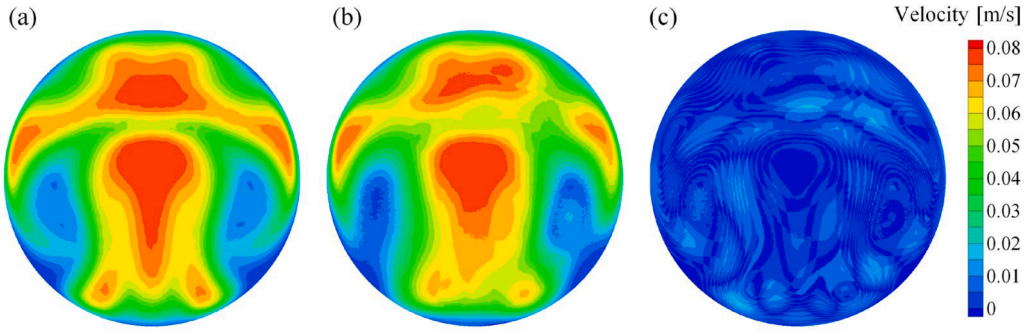

Fig. 22. Contours of velocity and absolute error at the observation section: (a) velocity by numerical simulation, (b) velocity by PIV experiment, and (c) absolute error.

Declaration of competing interest

The authors declare that they have no known competing financial interests or personal relationships that could have appeared to influence the work reported in this paper.

Acknowledgments

This work was supported by the National Key Research and Development Program of China (No. 2022YFB4003801).

References

[1] A. Hajatzadeh Pordanjani, S. Aghakhani, M. Afrand, B. Mahmoudi, O. Mahian, S. Wongwises, An updated review on application of nanofluids in heat exchangers for saving energy, Energy Convers. Manage. 198 (2019) 111886.
[2] S. Liu, M. Sakr, A comprehensive review on passive heat transfer enhancements in pipe exchangers, Renew. Sustain. Energy Rev. 19 (2013) 64–81.
[3] R. Barzegarian, A. Aloueyan, T. Yousefi, Thermal performance augmentation using water based Al 2 O 3 -gamma nanofluid in a horizontal shell and tube heat

exchanger under forced circulation, Int. Commun. Heat Mass Trans. 86 (2017) 52–59.
[4] L. Zhang, L. Tian, A. Zhang, H. Chen, Effects of the shape of tube and flow field on fluid flow and heat transfer, Int. Commun. Heat Mass Trans. 117 (2020) 104782.
[5] N. Zheng, P. Liu, F. Shan, Z. Liu, W. Liu, Effects of rib arrangements on the flow pattern and heat transfer in an internally ribbed heat exchanger tube, Int. J. Therm. Sci. 101 (2016) 93–105.
[6] B. Kumar, G.P. Srivastava, M. Kumar, A.K. Patil, A review of heat transfer and fluid flow mechanism in heat exchanger tube with inserts, Chem. Eng. Process. Process Intensif. 123 (2018) 126–137.
[7] M. Sheikholeslami, M. Gorji-Bandpy, D.D. Ganji, Review of heat transfer enhancement methods: focus on passive methods using swirl flow devices, Renew. Sustain. Energy Rev. 49 (2015) 444–469.
[8] K. Bilen, N. Tokgoz, İ. Solmaz, T. Balta, Thermo-hydraulic performance of tube with decaying swirl flow generators, Appl. Therm. Eng. 200 (2022) 117643.
[9] H. Bas, V. Ozceyhan, Heat transfer enhancement in a tube with twisted tape inserts placed separately from the tube wall, Exp. Thermal Fluid Sci. 41 (2012) 51–58.
[10] H.H. V, M. K, Heat and fluid flow behaviors in a laminar tube flow with circular protruded twisted tape inserts, Case Stud, Therm. Eng. 32 (2022) 101880.
[11] A.S. Dalkılıç, B. Uluç, M.S. Cellek, A. Celen, C. Jumpholkul, K.S. Newaz, S. Wongwises, Single phase flow heat transfer characteristics of quad-channel twisted tape inserts in tubes, Int. Commun. Heat Mass Trans. 118 (2020) 104835.
[12] X. Zhang, Z. Liu, W. Liu, Numerical studies on heat transfer and flow characteristics for laminar flow in a tube with multiple regularly spaced twisted tapes, Int. J. Therm. Sci. 58 (2012) 157–167.
[13] M.A. Akhavan-Behabadi, R. Kumar, M.R. Salimpour, R. Azimi, Pressure drop and heat transfer augmentation due to coiled wire inserts during laminar flow of oil inside a horizontal tube, Int. J. Therm. Sci. 49 (2010) 373–379.
[14] B. Ravikiran, K. Ramji, T. Subrahmanyam, Investigation on thermal performance of different wire coil twisted tape inserts in a tube circulated with water, Int. Commun. Heat Mass Trans. 122 (2021) 105148.
[15] P.W. Deshmukh, R.P. Vedula, Heat transfer and friction factor characteristics of turbulent flow through a circular tube fitted with vortex generator inserts, Int. J. Heat Mass Trans. 79 (2014) 551–560.
[16] J.-A. Meng, X.-G. Liang, Z.-X. Li, Field synergy optimization and enhanced heat transfer by multi-longitudinal vortexes flow in tube, Int. J. Heat Mass Trans. 48 (2005) 3331–3337.
[17] H. Jia, Z.C. Liu, W. Liu, A. Nakayama, Convective heat transfer optimization based on minimum entransy dissipation in the circular tube, Int. J. Heat Mass Trans. 73 (2014) 124–129.
[18] J. Wang, W. Liu, Z. Liu, The application of exergy destruction minimization in convective heat transfer optimization, Appl. Therm. Eng. 88 (2015) 384–390.
[19] W. Liu, P. Liu, J.B. Wang, N.B. Zheng, Z.C. Liu, Exergy destruction minimization: a principle to convective heat transfer enhancement, Int. J. Heat Mass Trans. 122 (2018) 11–21.
[20] N. Zheng, P. Liu, F. Shan, J. Liu, Z. Liu, W. Liu, Numerical studies on thermo-hydraulic characteristics of laminar flow in a heat exchanger tube fitted with vortex rods, Int. J. Therm. Sci. 100 (2016) 448–456.
[21] P. Liu, N. Zheng, F. Shan, Z. Liu, W. Liu, An experimental and numerical study on the laminar heat transfer and flow characteristics of a circular tube fitted with multiple conical strips inserts, Int. J. Heat Mass Trans. 117 (2018) 691–709.
[22] S. Chamoli, R. Lu, P. Yu, Thermal characteristic of a turbulent flow through a circular tube fitted with perforated vortex generator inserts, Appl. Therm. Eng. 121 (2017) 1117–1134.
[23] Y. Wang, P. Liu, H. Xiao, Z. Liu, W. Liu, Design and optimization on symmetrical wing longitudinal swirl generators in circular tube for laminar flow, Int. J. Heat Mass Trans. 193 (2022) 122961.
[24] P. Liu, N. Zheng, F. Shan, Z. Liu, W. Liu, Numerical study on characteristics of heat transfer and friction factor in a circular tube with central slant rods, Int. J. Heat Mass Trans. 99 (2016) 268–282.
[25] N. Zheng, F. Yan, K. Zhang, T. Zhou, Z. Sun, A review on single-phase convective heat transfer enhancement based on multi-longitudinal vortices in heat exchanger tubes, Appl. Therm. Eng. 164 (2020) 114475.
[26] X.W. Zhu, Y.H. Fu, J.Q. Zhao, A novel wavy-tape insert configuration for pipe heat transfer augmentation, Energy Convers. Manage. 127 (2016) 140–148.
[27] F.H. Sani, M. Pourfallah, M. Gholinia, The effect of MoS2–Ag/H2O hybrid nanofluid on improving the performance of a solar collector by placing wavy strips in the absorber tube, Case Stud, Therm. Eng. 30 (2022) 101760.
[28] Y. Liang, P. Liu, N. Zheng, F. Shan, Z. Liu, W. Liu, Numerical investigation of heat transfer and flow characteristics of laminar flow in a tube with center-tapered wavy-tape insert, Appl. Therm. Eng. 148 (2019) 557–567.
[29] S. Katoch, S.S. Chauhan, V. Kumar, A review on genetic algorithm: past, present, and future, Multimed Tools Appl 80 (2020) 8091–8126.
[30] Y. Ge, Z. Liu, F. Shan, F. Yuan, R. Long, W. Liu, Multi-objective arrangement optimization of a tube bundle in cross-flow using CFD and genetic algorithm, Energy Procedia 142 (2017) 3774–3779.
[31] T.S. Athith, G. Trilok, P.H. Jadhav, N. Gnanasekaran, Heat transfer optimization using genetic algorithm and artificial neural network in a heat exchanger with partially filled different high porosity metal foam, Mater. Today: Proc. 51 (2022) 1642–1648.
[32] H.C. Cui, C.Y. Shi, M.J. Yu, Z.K. Zhang, Z.C. Liu, W. Liu, Optimal parameter design of a slot jet impingement/microchannel heat sink base on multi-objective optimization algorithm, Appl. Therm. Eng. 227 (2023) 120452.
[33] M.N. Kuru, Optimization of heat and fluid flow over curved trapezoidal winglet pair type vortex generators with one-row and three-row, in: Heat Mass Transfer., 59, 2023, pp. 1437–1458.
[34] A. Abdollahi, M. Shams, Optimization of shape and angle of attack of winglet vortex generator in a rectangular channel for heat transfer enhancement, Appl. Therm. Eng. 81 (2015) 376–387.
[35] N. Zheng, P. Liu, F. Shan, Z. Liu, W. Liu, Sensitivity analysis and multi-objective optimization of a heat exchanger tube with conical strip vortex generators, Appl. Therm. Eng. 122 (2017) 642–652.
[36] A. Esmaeilzadeh, N. Amanifard, H.M. Deylami, Comparison of simple and curved trapezoidal longitudinal vortex generators for optimum flow characteristics and heat transfer augmentation in a heat exchanger, Appl. Therm. Eng. 125 (2017) 1414–1425.
[37] L. Shijie, Q. Zuoqin, W. Qiang, Optimization of thermohydraulic performance of tube heat exchanger with L twisted tape, Int. Commun. Heat Mass Trans. 145 (2023) 106842.
[38] C. Shi, Y. Zhu, M. Yu, Z. Liu, Arrangement optimization of spherical dimples inside tubes based on machine learning for realizing the optimal flow pattern, Therm. Sci. Eng. Prog. 44 (2023) 102065.
[39] C. Shi, M. Yu, W. Liu, Z. Liu, Shape optimization of corrugated tube using B-spline curve for convective heat transfer enhancement based on machine learning, Sci. China Technol. Sci. 65 (2022) 2734–2750.
[40] W.C. Reynolds, Heat Transfer to Fully Developed Laminar Flow in a Circular Tube With Arbitrary Circumferential Heat Flux, J. Heat Mass Trans. 82 (1960) 108–112.
[41] K. Dammak, A. El Hami, Thermal reliability-based design optimization using Kriging model of PCM based pin fin heat sink, Int. J. Heat Mass Trans. 166 (2021) 120745.
[42] L. Yicong, S. Chunyu, L. Wei, L. Zhichun, Structural parameter design of welded plate heat exchanger based on multi-objective optimization algorithm, Int. Commun. Heat Mass Trans. 146 (2023) 106900.
[43] Z. Zheng, X. Huang, Z. Jiang, Thermal performance and heat transfer reliability analysis in helically corrugated helical tube, Int. J. Therm. Sci. 183 (2023) 107849.
[44] Z.Y. Guo, W.Q. Tao, R.K. Shah, The field synergy (coordination) principle and its applications in enhancing single phase convective heat transfer, Int. J. Heat Mass Trans. 48 (2005) 1797–1807.
[45] W. Liu, Z. Liu, L. Ma, Application of a multi-field synergy principle in the performance evaluation of convective heat transfer enhancement in a tube, Chin. Sci. Bull. 57 (2012) 1600–1607.